Automated 4D Segmentation of Aortic Magnetic Resonance Images

Fei Zhao[1], Honghai Zhang[1], Andreas Wahle[1],
Thomas D Scholz[2], and Milan Sonka[1]
[1]Department of Electrical Engineering [2]Department of Pediatrics
University of Iowa
Iowa City, Iowa, USA
milan-sonka@uiowa.edu

Abstract

Automated and accurate segmentation of the aorta in 4D (3D+time) cardiovascular magnetic resonance (MR) image data is important for early detection of congenital aortic disease leading to aortic aneurysms and dissections. An automated 4D segmentation method is reported in this study. Our automated segmentation method combines level-set and optimal surface segmentation algorithms so that the final aortic surfaces in *n* cardiac phases are determined in a single optimization process. 4D MR image data sets acquired from 21 normal and connective tissue disorder subjects were used to evaluate the performance of our method. The automated 4D segmentation results produced accurate aortic surfaces in 16 cardiac phases, covering the aorta from the left-ventricular outflow tract to the diaphragm, yielding subvoxel accuracy with signed surface positioning errors of -0.07$\pm$1.16 voxel (-0.10$\pm$2.05 mm).

1 Introduction

Aortic aneurysms and dissections are the 15th leading cause of death in the US, representing 0.7% of all deaths in 2004. Persons with certain congenital connective tissue disorders, such as Marfan's Syndrome and Familial Thoracic Aortic Aneurysm Syndrome are at increased risk of developing aortic aneurysm and/or dissection. Therefore, early diagnosis of connective tissue disorders is increasingly important.

During the last decade, cardiovascular magnetic resonance (MR) imaging contributed substantially to the cardiovascular disease diagnosis. 4D cardiovascular MR image that consists of a sequence of 3D images throughout the cardiac cycle supplies important functional information about aortic motion, which is missing in single-phase 3D images. This information shall improve the diagnosis of the aortic disease. However, 4D MR image analysis is a nontrivial task. When attempting this task manually, obtaining reproducible tracings of the aorta in an n-phase 4D images requires expert knowledge and is tedious and time-consuming. Fig. 1 shows two images (middle 2D slice) with manually traced aorta contours randomly selected out of the 16 3D image sequences. Therefore, an automated 4D segmentation algorithm needs to be developed.

BMVC 2006 doi:10.5244/C.20.26

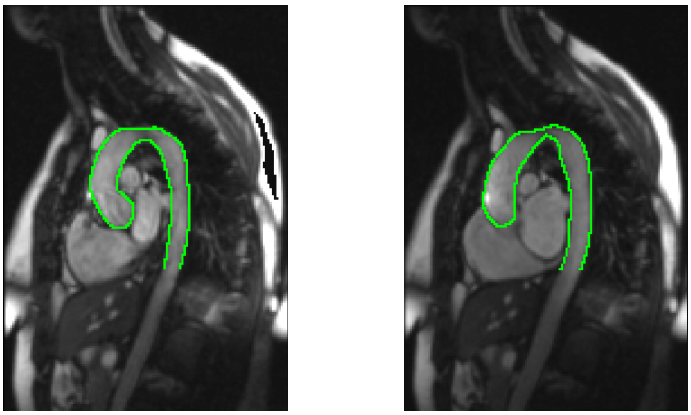

Figure 1: Middle slice of a 16-phase "candy cane" MR image, shown in two phases with manually traced aortic contours.

While a number of 3D aortic segmentation methods were reported [1, 2, 3] and others have developed methods for aortic motion tracking, to the best of our knowledge, no 4D method for accurate segmentation of the aorta has been presented to date. We report a highly automated 4D segmentation algorithm which can simultaneously segment a temporal (4D) sequence of 3D surfaces considering their temporal interrelations.

2 Methods

An *n*-phase 4D (spatial-temporal) image I can be viewed as a discrete set of n volumetric images defined at n different time instants $\{I_t(\mathbf{x},\mathbf{y},\mathbf{z})\}_{t\in[0,n-1]}$. The 4D aortic surface can be viewed as a sequences of surfaces $\{S_t\}_{t\in[0,n-1]}$. Our 4D segmentation algorithm consists of the following steps:

- *Aortic surface presegmentation:* A 4D fast marching level set method simultaneously yields approximate 4D aortic surfaces $\{appS_t\}_{t\in[0,n-1]}$.
- *Centerline extraction:* Aortic centerlines are determined from each approximate surface by skeletonization.
- *Accurate aortic surface segmentation:* Accurate 4D aortic surface $\{S_t\}_{t\in[0,n-1]}$ is obtained simultaneously with the application of a novel 4D optimal surface detection algorithm.

2.1 Aortic Surface Presegmentation

In order to presegment the 4D aortic image, 4D fast marching method was used [4]. Starting with an interactively identified seed point within the 4D aortic image, the initial surface propagates in an outward direction with speed F. Let $T_q(i,j,k)$ be the arrival time at which the level set surface passes through point (i,j,k,q) in the 4D image. The gradient

of this arrival time shall be inversely proportional to the speed function F [4]

$$|\nabla T| F = 1 \ . \tag{1}$$

The principal idea behind fast marching method is to trace the surface according to the solution function $T_q(i,j,k)$ solved using Eq. (1). The fast marching method consists of the following steps: 1) Add the seed point to set *Known*, add neighbor points to set *Trial*, add all other points to set *Far*. 2) Begin Loop: Find the point **P** with smallest T value in *Trial*, remove it from *Trial* and add it to *Known*. 3) Check all neighbor points of **P**; if the neighbor belongs to *Far*, remove it from *Far*, and add it to *Trial*. 4)Recalculate the T value for all neighbor points of **P** according Eq. (1). 5) Return to top of loop.

To improve the segmentation performance, a 3D vessel enhancement filter is first applied to the original image to suppress noise and image background for tubular objects [5]. Let G_s be the Gaussian-smoothed image with standard deviation s. Let the eigenvalues of the Hessian matrix $\nabla^2 G_s$ be λ_1, λ_2 and λ_3. The vesselness function is defined as:

$$V_t(x,y,z,s) = \begin{cases} 0 & \text{if } \lambda_2 > 0 \text{ or } \lambda_3 > 0 \\ (1-e^{R_A^2/2\alpha^2}) e^{R_B^2/2\beta^2} (1-e^{W^2/2\gamma^2}) & \text{otherwise} \end{cases} \tag{2}$$

where α, β and γ are parameters. In this study, $\alpha = 0.5$, $\beta = 0.5$, and γ was set as half the value of the maximum Hessian norm, and s denotes scale. The ratio R_A helps distinguish between plate-like and line-like structures and the second ratio R_B helps distinguish between blob-like and line-like structures.

$$R_A = \frac{|\lambda_2|}{|\lambda_3|}, \quad R_B = \frac{|\lambda_1|}{\sqrt{|\lambda_2 \lambda_3|}} \ . \tag{3}$$

The second order structureness W represents object deviation from the background

$$W = \sqrt{\sum_{j=1,2,3} \lambda_j^2} \ . \tag{4}$$

For the multiscale vessel filter, the vesselness generates maximum response at a scale which matches the diameter of the vessel to detect. The final vessel image $\{VI_t(\mathbf{x},\mathbf{y},\mathbf{z})\}_{t\in[0,n-1]}$ can be estimated as:

$$VI_t(x,y,z) = \max_{s_{min} \le s \le s_{max}} V_t(x,y,z,s) \ . \tag{5}$$

Using the vesselness image $VI_t(\mathbf{x},\mathbf{y},\mathbf{z})$, the vessel enhanced image $VEI_t(\mathbf{x},\mathbf{y},\mathbf{z})$ can be defined by Eq. (6), where θ is a noise/background suppression threshold which suppresses the noise and background. The speed function F can be defined by Eq. (7), where $G_\sigma * VEI_t(x,y,z)$ represents the image smoothed by a Gaussian filter with a characteristic width σ. This definition guides the surface development to stop at a high gradient

$$VEI_t(x,y,z) = \begin{cases} 0 & VI_t(x,y,z) < \theta \\ I_t(x,y,z) & \text{otherwise.} \end{cases} \tag{6}$$

$$F_t(x,y,z) = e^{-\alpha |\nabla (G_\sigma * VEI_t(x,y,z))|} \tag{7}$$

Using a binary tree sorting technique, the fast marching method solves Eq. (1) with time complexity of $O(N \log N)$, where N is the number of visited image points [4]. The

fast marching algorithm stops the surface in the vicinity of object boundaries, thus yielding the approximate object surface. In order to achieve an accurate segmentation, a skeletonization algorithm [6] is applied to the result of presegmentation to extract the aortic centerline for each phase.

2.2 Accurate Aortic Surface Segmentation

The 4D optimal surface detection algorithm uses a graph-based method consisting of *a*) coordinate transformation *b*) multi-surface detection using 4D optimal surface detection algorithm *c*) mapping of the segmentation result back onto the original image.

2.2.1 Coordinate Transformation

In order to construct the 4D aortic surface detection graph, a coordinate transformation is applied to each single phase image I_t. The cross sections are obtained by resampling the image using cubic B-spline interpolation in the plane perpendicular to the centerline [7]. The aorta is straightened by stacking the resampled cross sections to form a new volume. Each cross section in the resampled volume is unfolded into polar coordinates to transfer the cylindrical surface into a terrain-like surface [8]. This unfolded image is used for construction of the aortic surface detection graph. Fig. 2 shows the process of straightening the aorta into a cylindrical tube.

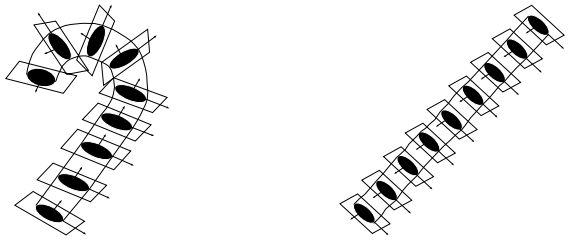

Figure 2: The process of transforming the aorta into a straight cylinder.

2.2.2 Segmentation of 4D Aortic Surface

After coordinate transformation, the desired 3D surfaces in an *n*-phase 4D aortic image are determined using the graph-based optimal surface segmentation algorithm [9]. Instead of resorting to a sequential segmentation of time series of 3D images, our segmentation method obtains a globally optimal 4D surface, where a sequence of 3D surfaces is segmented simultaneously and the temporal 3D surface interrelations are considered in a global optimization.

Graph Construction: Let $G = (V,E)$ be a connected, directed 4D graph constructed from an *n*-phase 4D image $\{I_t(\mathbf{x},\mathbf{y},\mathbf{z})\}_{t\in[0,n-1]}$. The vertex set V is represented by $\{V_t(\mathbf{x},\mathbf{y},\mathbf{z})\}_{t\in[0,n-1]}$. Considering each volumetric image as a 3D matrix with image sizes X, Y and Z in x, y and z direction, respectively, each vertex $V_t(x,y,z)$ in the 4D graph G corresponds to one voxel $I_t(x,y,z)$ of I. A cost, denoted by $c_t(x,y,z)$, is calculated and

assigned to each vertex. The lower the cost, the more likely it is that the vertex is on the surface. The arc set E consists of three types, intracolumn arcs E_a, intercolumn arcs E_r and intersurface arcs E_s.

Intracolumn arcs E_a: Let $Col_t(x,y)$ named (x,y) column represents the vertex subset $\{V_t(x,y,z)|z \in [0,Z-1]\}$. For each vertex in the column $Col_t(x,y)$, there is a directed arc connecting vertex $V_t(x,y,z)$ to vertex $V_t(x,y,z-1)$. Then, E_a is equal to $\{\langle V_t(x,y,z), V_t(x,y,z-1)\rangle \,|z>0\}$.

Intercolum arcs E_r: The terrain-like surface intersects with one vertex of each column $Col_t(x,y)$. The surface continuity in 3D is constrained by two smoothness parameters Δ_x, Δ_y. More specifically, if vertices $V_t(x,y,z)$ and $V_t(x+1,y,z')$ belong to the surface, $|z-z'| \leq \Delta_x$. Likewise, if vertices $V_t(x,y,z)$ and $V_t(x,y+1,z')$ belong to the surface, $|z-z'| \leq \Delta_y$. Since the terrain-like surface is unfolded from a cylindrical surface along the x direction, the first and last rows along the surface shall also satisfy the smoothness constrains. With these constrains, the intercolumn arcs E_r are defined as

$$E_r = \begin{cases} \{\langle V_t(x,y,z), V_t(x+1,y,\max(0,z-\Delta_x))\rangle \;|x \in [0,X-2], y \in \mathbf{y}, z \in \mathbf{z}\} \bigcup \\ \{\langle V_t(x,y,z), V_t(x-1,y,\max(0,z-\Delta_x))\rangle \;|x \in [1,X-1], y \in \mathbf{y}, z \in \mathbf{z}\} \bigcup \\ \{\langle V_t(x,y,z), V_t(x,y+1,\max(0,z-\Delta_y))\rangle \;|y \in [0,Y-2], x \in \mathbf{x}, z \in \mathbf{z}\} \bigcup \\ \{\langle V_t(x,y,z), V_t(x,y-1,\max(0,z-\Delta_y))\rangle \;|y \in [1,Y-1], x \in \mathbf{x}, z \in \mathbf{z}\} \bigcup \\ \{\langle V_t(0,y,z), V_t(X-1,y,\max(0,z-\Delta_x))\rangle \;|y \in \mathbf{y}, z \in \mathbf{z}\} \bigcup \\ \{\langle V_t(X-1,y,z), V_t(0,y,\max(0,z-\Delta_x))\rangle \;|y \in \mathbf{y}, z \in \mathbf{z}\} \end{cases}, \quad (8)$$

where $t \in [0,n-1]$.

Intersurface arcs E_s: Considering aortic motion information of the 4D image, surfaces in two consequent 3D images are interrelated. These temporal interrelation can be introduced by adding intersurface arcs E_s in the 4D graph. By doing so, a global optimization in 4D graph can be reached and therefore produces a 4D segmentation.

Intuitively, the terrain-like surfaces in two continuous phases can be viewed as a pair of interacting surfaces which cross each other within a specific distance range. Let S_t and S_{t+1} be two surfaces in two continuous phases G_t and G_{t+1} of the 4D graph G, and let $Col_t(x,y)$ and $Col_{t+1}(x,y)$ denote two corresponding columns in these two continuous 3D graphs. After assigning a pair of appropriate distance constraints δ_u and δ_l representing the maximum distance for the second surface with respect to the first surface, the intersurface arcs E_s are constructed as

$$E_s = \begin{cases} \{\langle V_t(x,y,z), V_{t+1}(x,y,\max(0,z-\delta_l))\rangle \;|x \in \mathbf{x}, y \in \mathbf{y}, z \in \mathbf{z}\} \bigcup \\ \{\langle V_{t+1}(x,y,z), V_t(x,y,\max(0,z-\delta_u))\rangle \;|x \in \mathbf{x}, y \in \mathbf{y}, z \in \mathbf{z}\}. \end{cases}, \quad (9)$$

where $t \in [0,n-1]$. The construction of E_s guarantees that if the vertex $V_t(x,y,z)$ is on S_t, then it's correspondence vertex on S_{t+1} must be no further than vertex $V_{t+1}(x,y,\max(0,z-\delta_l))$. Similarly, if the vertex $V_{t+1}(x,y,z)$ is on S_{t+1}, then it's correspondence vertex on S_t must be no further than vertex $V_t(x,y,\max(0,z-\delta_u))$. The distance constraints δ_u and δ_l are determined by the aortic motion change in two continuous phases. In this study, $\delta_u = 5$ and $\delta_l = 5$. Fig. 3(a) shows an example of intracolumn and intercolumn arcs, Fig. 3(b) shows example of intersurface arcs.

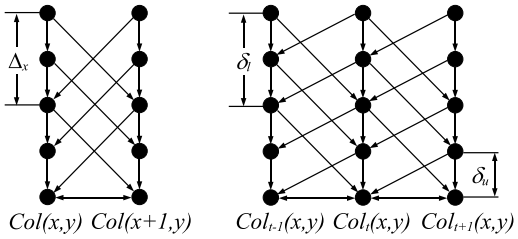

Figure 3: An example of graph construction. (a) An example of intracolumn and intercolumn arcs. (b) An example of intersurface arcs.

Optimization: After constructing the 4D graph, the surface detection problem is transformed into a search for the minimum closed set [10] in a weighted graph by assigning the weight of each vertex as

$$w_t(x,y,z) = \begin{cases} c_t(x,y,z) & \text{if } z = 0 \\ c_t(x,y,z) - c_t(x,y,z-1) & \text{otherwise.} \end{cases} \tag{10}$$

The minimum closed set problem can be solved by using the minimum *s–t* cut algorithm presented in [9].

2.2.3 Cost function design

Since the ascending aorta is connected to the left ventricle and is surrounded by tissues of similar MR appearance as the aortic wall, the aortic surface is difficult to detect using a simple cost function. Therefore, two different cost functions were developed – one for the ascending aorta and the other for the descending aorta. First, an edge image of the aorta is computed from the straightened image data. The usual simple edge operators often overestimate or underestimate the actual border positions. To overcome this problem, we have used a previously developed approach, which utilizes a combination of first and second derivatives (3×3 Sobel edge detector and 5×5 Marr-Hildreth edge detector) in the individual cross sections. The edge image is then

$$EI = (\alpha S + \beta M) I_{2D} \ , \tag{11}$$

where I_{2D} is the 2D cross section of the original image, S is the Sobel operator, and M is the Marr-Hildreth operator. The parameters α and β control the relative weights of the first and second derivatives, respectively. For our MR data, $\alpha = 0.8$ and $\beta = 0.2$. The cost function was formed as follows:

$$Cost(i,j) = \max_{x \in \mathbf{x}, y \in \mathbf{y}} \{\overline{EF}(x,y)\} - \overline{EF}(i,j) \ , \tag{12}$$

where $\overline{EF}(i,j)$ is the edge function which is inverted to the cost function.

Descending Aorta and Aortic Arch: Let $d(i,j)$ represent the edge direction of a pixel (i,j). The edge function for the descending aorta and the aortic arch $\overline{EF}_d$ is defined as

$$\overline{EF}_d(i,j) = \begin{cases} EI(i,j) & d(i,j) \in [\pi/2, 3\pi/2] \\ EI(i,j) - \Delta P & \text{otherwise} \end{cases} \ , \tag{13}$$

where ΔP is a constant penalty term.

Ascending Aorta The ascending aorta surfaces require a knowledge-based cost function. After examining the cross section perpendicular to the centerline, a small gap between the ascending aorta border and its surrounding tissue is detected. The thickness of this gap ranges from 2 to 4 pixels. Using this information, the edge function of the ascending aorta $\overline{EF}_a$ is calculated as a combination of two related edges:

$$\overline{EF}_a(i,j) = \overline{EF}_i(i,j) + \overline{EF}_o(i,j) \ . \tag{14}$$

The inner border edge function $\overline{EF}_i(i,j)$ and outer border edge function $\overline{EF}_o(i,j)$ are

$$\overline{EF}_i(i,j) = \begin{cases} EI(i,j) & \text{if } d(i,j) \in [\pi/2, 3\pi/2] \\ EI(i,j) - \Delta P & \text{otherwise} \end{cases} \ , \tag{15}$$

$$\overline{EF}_o(i,j) = \max_{\Delta j=2,3,4} \begin{cases} EI(i,j+\Delta j), & \text{if } d(i,j+\Delta j) \in [-\pi/2, \pi/2] \\ EI(i,j+\Delta j) - \Delta P, & \text{otherwise .} \end{cases} \tag{16}$$

3 Experimental Methods

3.1 Image Data Acquisition

The algorithm was evaluated in a set of 21 MR image sequences acquired from 21 subjects (14 normal, 7 patients). Each sequence was composed of 16 cardiac phases covering one cardiac cycle. For each subject the candy cane view is captured with voxel sizes ranging from $1.5 \times 1.5 \times 3.0\,\text{mm}^3$ to $2.0 \times 2.0 \times 6.0\,\text{mm}^3$. The patients were selected due to their family history of connective tissue disorder.

3.2 Study Protocol and Data Analysis

To assess the accuracy of the automated 4D segmentation, aortic luminal surfaces were compared with the expert traced independent standard. The independent standard was defined by manual tracing in 5 randomly selected phases in each of the 21 subjects (7 patients and 14 normal subjects, total of 420 manually traced slices). Surface positioning errors were defined as the shortest distances between the manually traced and computer-determined surfaces in the 4D aortic images. Signed and unsigned surface positioning errors are expressed as mean$\pm$standard deviation in voxels and millimeters. Every location whose unsigned surface positioning error exceeds 4 mm was recorded, and reported to the expert observer – an experienced cardiologist. The observers then checked those locations and determined whether the positioning error was introduced by manual tracing or the segmentation algorithm.

4 Results

All 21 4D aortic MR images were successfully segmented by our 4D segmentation algorithm. Comparison of computer-determined and expert-traced surfaces showed good

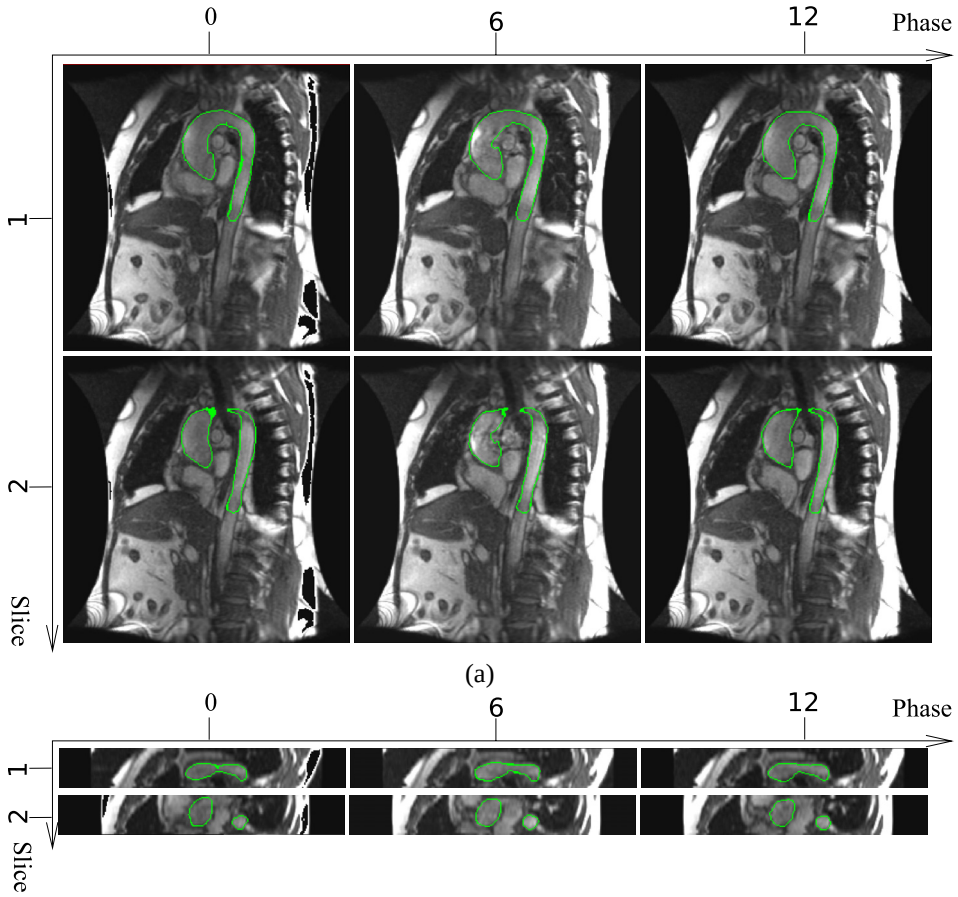

Figure 4: Automated 4D segmentation result. For each view shown in the figure, three phases (0, 6, 12) were selected from the 4D image, and two 2D slices were selected for each single phase. The horizontal coordinates represent the phase number, the vertical coordinates represents the slice number. (a) Transverse view. (b) Coronal view.

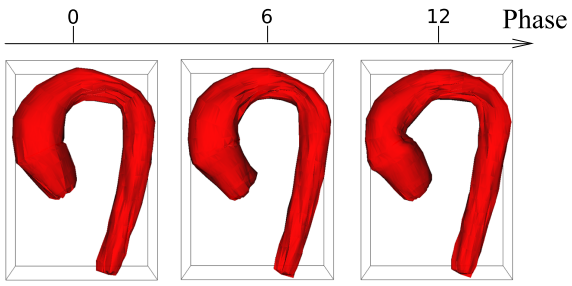

Figure 5: Volumetric representation of computer-based aortic segmentation.

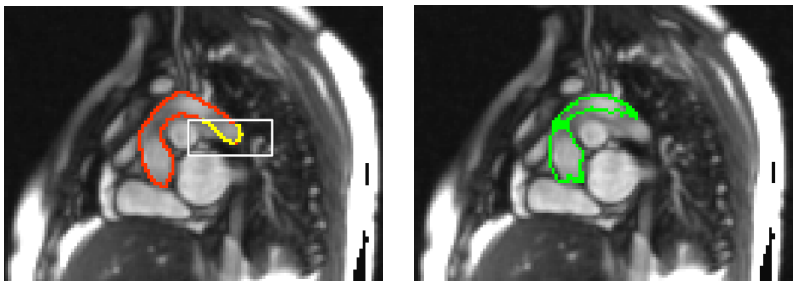

(a) (b)

Figure 6: The manual tracing boundary and the automated segmentation result on the same slice. (a) Expert-identified boundary. Note that the manually traced boundary shown inside the box has the positioning error larger than 4 mm due to tracing an adjacent structure by mistake. (b) Computer segmentation showing correctly identified aortic boundary.

agreement. The segmentation produced aortic surfaces with subvoxel accuracy as judged by the signed surface positioning errors of -0.07$\pm$1.16 voxel (-0.10$\pm$2.05 mm) and unsigned positioning errors of 0.88$\pm$0.807 voxel (1.55$\pm$1.44 mm). An example of a typical 4D segmentation result is shown in Fig. 4. The segmentation result is shown in transverse and coronal views (Figs. 4(a), (b), respectively). The volumetric representation of segmentation is shown in Fig. 5.

In these 21 subjects, 43 suspicious locations with unsigned surface positioning error exceeding 4 mm were recorded. After their examination, the expert found that aortic surfaces were incorrectly manually identified in 40 of the 43 locations. Fig. 6 shows us the manually traced boundary and the computer segmentation result in comparison. Fig. 6(b) shows the aorta boundary generated by our segmentation algorithm. After checking this suspicious location, the expert observer determined that the portion of the boundary within the box in Fig. 6(a) belonged to another vessel very close to the aorta. Such errors are inherent to manual tracing and demonstrate the difficulty of visual analysis. Fig. 6(b) shows that our method can effectively eliminate these mistracing problems by taking 3D context into consideration.

5 Discussion and Conclusion

In this study, an automated 4D segmentation algorithm which combines a 4D fast marching level-set segmentation with an optimal graph-based multiple surface detection algorithm was presented. This algorithm provides accurate and reliable aortic surfaces. The novelty of the segmentation algorithm lies in combining the 4D fast marching algorithm with optimal graph-based multiple surfaces detection algorithm.

The use of the 4D fast marching algorithm provides an automated presegmentation of the aorta allowing determination of the aortic centerline. Using the centerline, optimal graph-based multiple surfaces detection algorithm generates accurate and robust 4D segmentation surfaces with a single global optimization on the 4D aortic MR images. The resulting aortic surfaces showed an excellent agreement with the segmentations traced by expert observers. Importantly, we demonstrated that most 40 of the gross errors ini-

tially detected in the validation were caused by imperfections of our independent standard further demonstrating the value of our reported approach.

References

[1] D. Rueckert, P. Burger, S. Forbat, R. Mohiaddin, and G. Yang, "Automatic tracking of the aorta in cardiovascular MR images using deformable models," *IEEE Transactions on Medical Imaging*, vol. 16, no. 5, pp. 581–590, 1997.

[2] T. Behrens, K. Rohr, and H. Stiehl, "Robust segmentation of tubular structures in 3D medical images by parametric object detection and tracking," *IEEE Transactions on Systems, Man, and Cybernetics*, vol. 33, no. 4, pp. 554–561, 2003.

[3] M. de Bruijne, B. van Ginneken, M. A. Viergever, and W. J. Niessen, "Adapting active shape models for 3D segmentation of tubular structures in medical images," in *Proc. of IPMI*, vol. 2732 of *LNCS*, pp. 136–147, Springer-Verlag, 2003.

[4] R. Malladi and J. A. Sethian, "A real-time algorithm for medical shape recovery," in *Proc. of ICCV*, pp. 304–310, IEEE Computer Society Press, 1998.

[5] A. Frangi, W. Niessen, K. Vincken, and M. Viergever, "Multiscale vessel enhancement filtering," in *Proc. of MICCAI*, vol. 1496 of *LNCS*, pp. 130–137, Germany: Springer-Verlag, 1998.

[6] K. Palagyi, E. Sorantin, E. Balogh, A. Kuba, C. Halmai, B. Erdhelyi, and K. Hausegger, "A sequential 3D thinning algorithm and its medical applications," in *Proc. of IPMI*, vol. 2082 of *LNCS*, pp. 409–415, Springer-Verlag, 2001.

[7] M. Unser, A. Aldroubi, and M. Eden, "B-spline signal processing: Part I - theory," *IEEE Transactions on Signal Processing*, vol. 41, no. 2, pp. 821–833, 1993.

[8] M. Sonka, V. Hlavac, and R. Boyle, *Image Processing, Analysis, and Machine Vision*. PWS, 1998.

[9] K. Li, X. Wu, D. Z. Chen, and M. Sonka, "Optimal surface segmentation in volumetric images - a graph-theoretic approach," *IEEE Transactions on Pattern Analysis and Machine Intelligence*, vol. 28(1), pp. 119–134, 2006.

[10] X. Wu and D. Z. Chen, "Optimal net surface problems with applications," in *Proc. of ICALP*, vol. 2380 of *LNCS*, pp. 1029–1024, Springer-Verlag, 2002.